

Contents lists available at ScienceDirect

## Journal of the Mechanical Behavior of Biomedical Materials

Journal of het.
Mechanical Behavior of
Biometical Materials

journal homepage: www.elsevier.com/locate/jmbbm



# Measuring viscoelastic parameters in Magnetic Resonance Elastography: a comparison at high and low magnetic field intensity

Marco Andrea Zampini a,b,c,\*, Martina Guidetti , Thomas J. Royston , Dieter Klatt

- <sup>a</sup> University of Illinois at Chicago, Department of Bioengineering, University of Illinois at Chicago, Chicago, IL, 60607, USA
- <sup>b</sup> MR Solutions Ltd, Ashbourne House, Old Portsmouth Rd, Guildford, United Kingdom
- <sup>c</sup> Bio-Imaging Lab, Department of Biomedical Sciences, University of Antwerp, Universiteitsplein 1, Wilrijk, Belgium

## ARTICLE INFO

#### Keywords:

Magnetic Resonance Elastography (MRE) Complex shear modulus Tabletop MRI Rheological models

## ABSTRACT

Magnetic Resonance Elastography (MRE) is a non-invasive imaging technique which involves motion-encoding MRI for the estimation of the shear viscoelastic properties of soft tissues through the study of shear wave propagation. The technique has been found informative for disease diagnosis, as well as for monitoring of the effects of therapies. The development of MRE and its validation have been supported by the use of tissue-mimicking phantoms. In this paper we present our new MRE protocol using a low magnetic field tabletop MRI device at 0.5 T and sinusoidal uniaxial excitation in a geometrical focusing condition. Results obtained for gelatin are compared to those previously obtained using high magnetic field MRE at 11.7 T. A multi-frequency investigation is also provided via a comparison of commonly used rheological models: Maxwell, Springpot, Voigt, Zener, Jeffrey, fractional Voigt and fractional Zener. Complex shear modulus values were comparable when processed from images acquired with the tabletop low field scanner and the high field scanner. This study serves as a validation of the presented tabletop MRE protocol and paves the way for MRE experiments on ex-vivo tissue samples in both normal and pathological conditions.

#### 1. Introduction

Elastography is a non-invasive imaging technique for the estimation of shear viscoelastic properties in soft tissues (Yamakoshi et al., 1990; Parker et al., 1990; Krouskop et al., 1987; Emelianov et al., 1995; Sarvazyan et al., 2011, 2013; Muthupillai et al., 1995) and is related to manual palpation, a fundamental step in a clinical physical evaluation. Elastography techniques can be classified into quasi-static and dynamic approaches (Varghese, 2009): while the former apply a time-invariant force to the tissue, the latter use a time-varying force that results in the propagation of mechanical waves, both of the compressional and shear kinds (Taljanovic et al., 2017). Dynamic elastography techniques observe shear wave propagation and produce quantitative stiffness maps compared to quasi static methods that only quantify contrast (relative stiffness values), without quantitative information about boundary conditions (Klatt et al., 2010a; Gennisson et al., 2013). Elastography measurements can be made using different imaging modalities, such as ultrasound (Yamakoshi et al., 1990; Parker et al., 1990; Dutt et al., 2000; Deffieux et al., 2011; Wang et al., 2013), optics (Von Gierke et al., 1952; Liang and Boppart, 2009; Larin and Sampson, 2017; Khan et al., 2018),

or magnetic resonance imaging (MRI) (Muthupillai et al., 1995; Plewes et al., 1995); in particular, the last approach is referred to as Magnetic Resonance Elastography (MRE), which involves motion-encoding MRI. MRE offers resolution up to hundreds of micrometers (Hiscox et al., 2018; Hughes et al., 2015), great penetration depth (Guidetti and Royston, 2018) and added value in a multiparametric MRI approach (Low et al., 2016). MRE has high diagnostic accuracy for the staging of hepatic fibrosis (Talwalkar, 2008) and has diagnostic potential for the detection of breast (Balleyguier et al., 2018), thyroid (Bahn et al., 2009) and prostate cancers (Reiter et al., 2020; Kemper et al., 2004). Promising studies on kidney (Lee et al., 2012), brain (Xu et al., 2007), heart (Sack et al., 2009) and muscle (Basford et al., 2002) tissues have also been reported. The development of these MRE approaches and their validation have been supported by the use of tissue-mimicking phantoms.

Phantoms play an essential role in the development of elastography: given their accessibility and convenience, they have been used as a means of standardization and validation (Mun et al., 2013), and they have also been employed to improve the performance and reliability of inversion algorithms to obtain material properties maps, called elastograms (Nguyen et al., 2014; Cao et al., 2017; Muthupillai et al., 1995),

<sup>\*</sup> Corresponding author. MR Solutions Ltd, Ashbourne House, Old Portsmouth Rd, Guildford, GU3 1LR, United Kingdom. E-mail address: marco.zampini@mrsolutions.com (M.A. Zampini).

and to evaluate motion acquisition approaches (Kolipaka et al., 2009; Klatt et al., 2013). Thus, scientific literature contains many studies about phantom materials: the reviews by Cao et al. (2017) and Culjat et al. (2010) classify the different types of tissue mimicking materials and describe their fabrication, benefits and disadvantages. Gelatin is the most common tissue substitute used in investigations (Amador et al., 2011; Quan et al., 1993; Doyley et al., 2001; Hall et al., 1997). Doyley et al. have used gelatin phantoms for assessing the quality of elastograms produced using an innovative imaging system for clinical breast elastography (Doyley et al., 2001), while Hall proposed numerous mechanical tests of tissue-like gelatin materials for elastography experiments (Hall et al., 1997). Other examples of materials used for tissue-like phantoms are agar-agar gel (Hamhaber et al., 2003; Manduca et al., 2001; Zell et al., 2007), agar-gelatin (Plewes et al., 2000; Madsen et al., 2005; Ringleb et al., 2005; Pavan et al., 2010), ecoflex (Brinker and Klatt, 2016; Brinker et al., 2018), polyurethane gel (Madsen and Frank, 1997), oil in gelatin (Madsen et al., 2003; Nguyen et al., 2014), aqueous polyvinyl alcohol solutions (Mori et al., 1997; Zell et al., 2007), silicone (Zell et al., 2007), polyacrylamide gel (Zell et al., 2007), glycerol in oil-based gel (Cabrelli et al., 2017), paraffin gel (Vieira et al., copolymer in oil styrene-ethylene/butylene-styrene (Oudry et al., 2009).

Customarily, MRE on phantoms has been performed using MRI scanners at high ( $B_0 > 1$  T (Oudry et al., 2009; Hamhaber et al., 2003; Ringleb et al., 2005)) and ultra-high ( $B_0 > 7$  T (Guidetti et al., 2019; Yasar et al., 2013)) magnetic field, taking advantage of the high sensitivity resulting in increased resolution and Signal-to-Noise Ratio (SNR) and reduced scan time (Ladd, 2007) compared to using scanners at low magnetic field. Nevertheless, both ultra-high and high magnetic field scanners come with high costs and are extremely bulky, thus requiring large magnet rooms. A higher field strength results in longer T1 relaxation times and thus longer repetition times in most of the pulse sequences for accurate relaxometry mapping (Bottomley et al., 1984). The chemical shift artifact is particularly evident as well, especially along the readout direction and this pitfall may necessitate either increasing the readout bandwidth or switching to fat suppression techniques, which can lead to Specific Absorption Rate (SAR) issues. Recently, a setup based on a 0.5 T tabletop MRI scanner was used for investigations of viscoelastic properties of small ex-vivo tissue samples and gel phantoms through MRE (Ipek-Ugay et al., 2015; Braun et al., 2018). With a permanent magnet in a tabletop device, the paradigm shift to the low field imaging comes with advantages: lower initial purchase price, operational and maintenance costs, lower fringe field effects - so a lower projectile risk and easier field shielding - as well as the decrease of chemical shift and susceptibility artifacts.

In this paper we present our new MRE protocol using a low magnetic field tabletop MRI device at 0.5 T and sinusoidal uniaxial excitation in a geometrical focusing condition. Results obtained for gelatin are compared to previously implemented ultra-high magnetic field MRE at 11.7 T. A multi-frequency investigation at 0.587 T is also provided via a comparison of commonly used rheological models. This study serves as a validation of the presented tabletop MRE protocol and paves the way for MRE experiments on ex-vivo tissue samples in both normal and pathological conditions.

## 2. Materials and methods

#### 2.1. Materials

A total of 5 samples for each of the 4 concentrations of gelatin solutions – 5%, 10%, 15% and 20% weight over volume (w/v) – were prepared with the intent to span over the shear stiffness range of biological tissue by solubilization of Gelatin Powder (IS16003, Lab Grade, Innovating Science <sup>TM</sup>, Aldon Corporation, Avon, NY) in distilled water and inserted in glass test tubes of 8 mm inner diameter (Amador et al., 2011). Within the deformation regime of MRE, gelatin – as soft tissues –

can be modeled as linear viscoelastic materials which are characterized by a storage modulus and a loss modulus ((Ortiz and Lagos, 2015; Yang and Church, 2006; Zhang et al., 2007; Maccabi et al., 2018)). The material is considered as nearly incompressible with a Poisson's ratio approxim able to 0.5 and with density of water ( $\rho = 1000 \, \text{kg/m}^3$ ). Given these assumptions, the relationship between Young's modulus E and shear modulus  $\mu$  is  $E \sim 3\mu$ .

## 2.2. Experimental setup

MRE experiments at low magnetic field were performed using a 10 mm diameter vertical bore tabletop MR scanner with a 0.5 T permanent magnet (MagSpec, Pure Devices GmbH, Würzburg, Germany). The scanner is controlled by a driver console (drive L, Pure Devices GmbH, Würzburg, Germany), requiring a licensed version of MATLAB (Mathworks, Natick, MA, USA) not older than Version 2012a. An external gradient amplifier (DC 600, Pure Devices GmbH, Würzburg, Germany) and an integrated custom-built piezoelectric actuator system were added to the setup (see Table 1). A similar system was used in the studies of Ipek-Ugay et al. (2015) and Braun et al. (2018).

Our setup includes a custom-made piezoelectric actuator support, as shown in Fig. 1, which is made of polycarbonate characterized by very low relative magnetic permeability, high density, high Poisson ratio and high Young's modulus: it has been designed using SolidWorks (Dassault Systèmes, Vélizy-Villacoublay, France) with the aim of building a highinertial, deformation-resistant and durable support at low cost. The components of the support were first fabricated separately and then chemically bonded; the support is provided with two flat sustains that touch the upper case of the scanner and with two holes on the lateral blocks hosting plastic screws, so that possible movements of the scanner are rigidly transferred to the support. The hollowed top block hosts the actuator in its cavity, with a H6 ISO tolerance to ensure the lowest clearance and, thus, an axial transmission of the displacement provided by the actuator through a threaded rod (hooking the sample tube extremity at one end and screwed in the actuator at the other end). The piezoelectric driver has an external diameter of 20 mm and a length of 72 mm. MRE at 0.5 T was followed by a comparison at ultra-high

**Table 1**Experimental parameters for the three scanners used in this study. For the sake of simplicity, we report the magnetic field intensities of the scanners truncated at the first decimal digit throughout the text.

Parameter	MagSpec (Pure Devices)	310/ASR (Agilent)	Advance III HD (Bruker)
Magnetic Field [T]	0.587 (25 MHz)	9.4 (400 MHz)	11.74 (500 MHz)
Piezoelectric actuator	PAHL 60/20 (*)	P-840.1 (**)	1000/50 N (**)
Oscillation amplitude [µm]	6	6	11
Excitation and MEG	[0.5, 1.0, 1.5,	[0.5, 1.0, 1.5,	[1.0, 2.0, 3.0,
frequencies [kHz]	2.0]	2.0]	4.0]
FOV dimensions	$10~\text{mm}\times10$	$68~mm \times 68$	10 mm x 10
	mm	mm	mm
Inner/Outer sample bin diameter [mm]	8/10	58/62	8/10
Matrix size	$128 \times 128$	64 × 64	$128 \times 128$
Spatial resolution [ $\mu$ m]	$78 \times 78$	$1063 \times 1063$	$78 \times 78$
Slice thickness [mm]	5	1	1
Slice volume [mm <sup>3</sup> ]	251.3	2642.1	50.3
MEG strength [mT/m]	200	250	1200
TE/TR [s/s]	0.0358/0.5	0.02128/1	0.00395/0.12
MEG duration [ms]	20	16	2
Number of averages	2	1	1
Scan time/frequency	$\sim 11 \text{ min}$	~9 min	~5 min
MRE sequence	SE-based	SLIM-MRE	SLIM-MRE

<sup>(\*)</sup> Piezosystem Jena, Jena, Germany. (\*\*) Physik Instrumente GmbH & Co., Karlsruhe, Germany.

SLIM = SampLe Interval Modulation, SE = Spin-Echo.

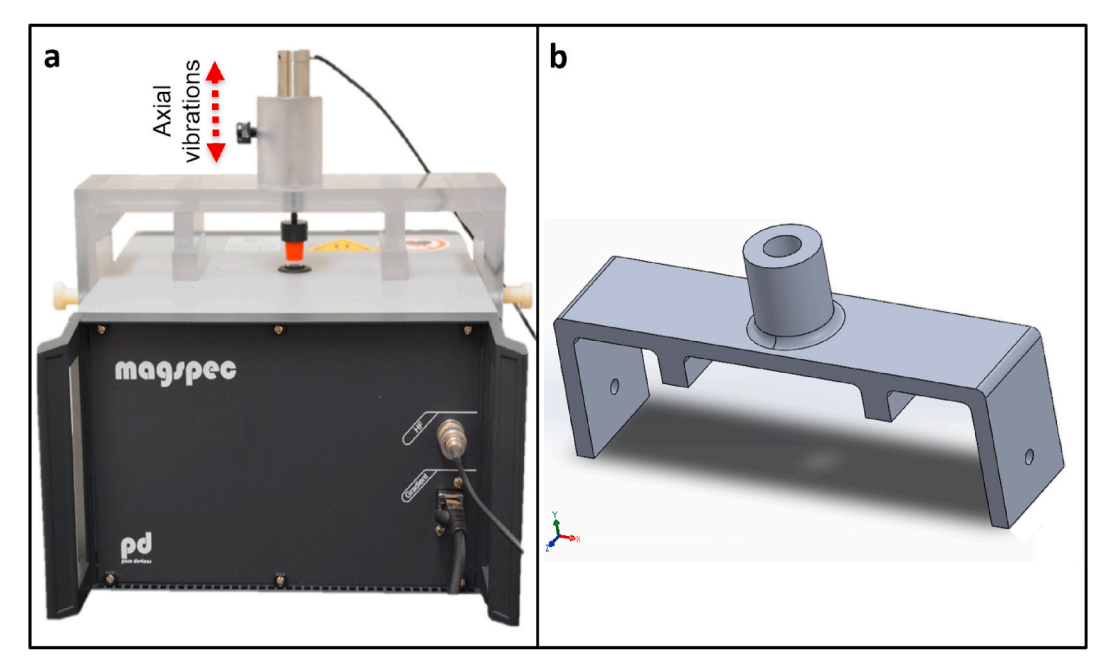


Fig. 1. (a) Picture of the MRE setup for piezoelectric actuator support mounted on the tabletop MRI machine by Pure Devices GmbH, Würzburg, Germany. (b) SolidWorks model of the piezoelectric actuator support.

magnetic field using the experimental setups of MRE described in previous publications (Reiter et al., 2020; Kearney et al., 2017; Yasar et al., 2013; Guidetti et al., 2019). These experiments were performed on a 56 mm vertical bore MR scanner (Bruker 11.7 T, Billerica, MA) and on a 310 mm horizontal bore MR Scanner (Agilent 9.4 T 310/ASR, Santa Clara, CA) with the same setup as in Yasar et al. (2013). A total of 3 samples with 3 concentrations – 5%, 10% and 15% w/v – were prepared for the 11.7 T experiments, similarly as discussed for tabletop experiments. At 9.4 T we acquired data from a single sample with 10% w/v concentration only as a validation at that specific concentration.

## 2.3. MRE experiments

The piezoelectric driver was fed with a sinusoidal alternating current with a vibration-amplitude dependent voltage (maximum 90 V) and 4 driving frequencies (f = 500, 1000, 1500 and 2000 Hz). The range of frequencies was chosen on the basis of the study of Guidetti et al. (2019), by which the lower bound frequency is chosen relying on the ratio of the test tube diameter to the wavelength. This makes sure that at least half a wavelength can be detected for the reconstruction procedure. On the other hand, the higher frequency limit is selected based on the attenuation given by the damping effect. In order to encode vibrations into the MRI phase map values using a spin echo pulse sequence, the sinusoidal excitation provided by the actuator was synchronized to the application of a bipolar 8-lobes trapezoidal motion-encoding gradient (MEG). Data acquisition was performed during the echo formation after switching off both the MEG and the mechanical excitation. Complex phase subtraction was performed to correct for static phase offsets, requiring two acquisitions with inverse-polarity MEGs at each of the four time instances per frequency.

The vibrations inside the test tube were polarized along the main axis of the cylinder due to the constrained axial motion direction of the actuator (Fig. 1a). Shear waves were introduced into the samples from the cylinder walls by producing concentric cylinder waves propagating from the outer sample boundaries towards the central axis of the test tube. This setup allowed the motion field acquisition to be limited by uniaxial z-component encoding and represented the geometric focusing technique (Yasar et al., 2013), which compensates for the damping effect due to the viscoelastic properties of the analyzed materials. When a

viscoelastic isotropic material is considered, the cylindrical coordinate wave equation provides the out-of-plane displacement  $u_z$  as a function of the radial position  $r\!:$ 

$$u_z(r,t,k_\beta) = u_{za} \frac{J_0(k_\beta r)}{J_0(k_\beta a)} e^{i\omega t}$$

$$\tag{1}$$

with  $u_{za}$  being the oscillation amplitude for r=a,  $k_{\beta}=\omega\sqrt{\frac{\rho}{\mu_R+j\mu_I}}$  being the shear wave number,  $J_0(z)$  the Bessel function of the first kind  $0^{th}$  order, with  $j=\sqrt{-1}, \rho$  the density,  $\omega$  the angular frequency,  $\mu_I$  and  $\mu_R$  referring to the imaginary and real part of the complex shear modulus  $\mu$  respectively, a being the radius of the test tube, and  $u_{za}$  the amplitude of the harmonic excitation set on the boundary by the piezoelectric actuator.

For MRE at 9.4 T and at 11.7 T a similar kind of sample materials and similar actuation setups were used as for the low field MRE experiments, with different piezoelectric actuators and MRE sequences and adjusted container dimensions. When using the SLIM-MRE sequence (Klatt et al., 2013), the motion was encoded by concentrating the gradient power in the slice direction and setting to zero the gradient amplitudes along the other two directions. A complete list of the acquisition parameters can be found in Table 1.

## 2.4. Data processing and analysis

Complex wave images were taken from the first harmonic after applying a discrete Fourier transform of the MR phase-difference images along the four time instances. For isotropic and homogeneous materials, the diameter profiles – lines representing the out-of-plane complex displacement crossing the center of the sample – can be used to estimate  $\mu(\omega)$  at different frequencies by matching the analytical closed form solution in Equation (1). Subsequently, rheological model parameters can be fit to the complex shear modulus when MRE is performed at multiple frequencies. With respect to propagation of shear waves over a broad frequency range, linear viscoelastic materials such as tissues and gelatin phantoms generally show an increase of shear storage and loss moduli with excitation frequency (Yasar et al., 2013; Guidetti et al., 2019; Klatt et al., 2010a; Liu et al., 2014). The displacement profiles were acquired along 4 arbitrary directions with equispaced angles.

Standard deviation was defined over the four fitted profiles at each excitation frequency and median-averaged over the samples with the same concentration. The complex modulus was computed by fitting the analytical closed solution to the real and imaginary parts of the complex displacement profiles through a constrained least-square optimization for a minimum search performed using the fmincon MATLAB function. To compare the SNR among different scanners, we computed the Coefficient of Variation (CV) as the standard deviation over the mean of the values of the magnitude of the displacement along each visible circular wave crest. Wave crests were automatically detected as displacement local maxima along a diameter after using a 3 pixel moving-average.

The mechanical behavior of soft tissues and their mimicking phantoms can be modeled through linear viscoelasticity when assuming the small deformation regime of MRE; the constitutive equations of rheological models are obtained by the combination of basic elements in serial or parallel arrangements. It is preferable to minimize the number of independent parameters in the constitutive model that is used (Sack et al., 2013). Constitutive models incorporating fractional derivative elements in them have been shown to optimally describe dynamic behavior of such materials using a minimal number of independent parameter (Bagley and Torvik, 1983; Pritz, 2003; Taylor et al., 2002; Chen et al., 2003; Kiss et al., 2004). Essentially, a generalization of conventional viscoelastic models is obtained by using a fractional basic rheological element, commonly referred to as the springpot, in addition to the spring and the dashpot. The springpot is described by two independent parameters. The first is  $\mu_{\alpha}$ , and the second is  $\alpha$  (0  $\leq \alpha \leq$  1), which is an interpolation parameter that represents the matrix geometry and varies between the pure elastic ( $\alpha = 0$ ) and viscous ( $\alpha = 1$ ) cases. The complex modulus of the springpot in the frequency domain is simply given as

$$\mu_a^{1-\alpha}(j\omega\mu_0)^\alpha , \qquad (2)$$

where  $j = \sqrt{-1}$ ,  $\omega$  is the circular frequency in radians/second and  $\mu_0$  is support variable typically set to 1 Pa·s (Yasar et al., 2013).

The storage and loss moduli of the springpot by itself are the real and imaginary parts, respectively, of this expression. Combining the springpot with other basic elements, such as springs, dashpots or additional springpots leads to a variety of rheological models with anywhere from 2 (springpot by itself) to more independent parameters. Some commonly used rheological models, with and without the springpot,

include the following: springpot by itself, Maxwell, Voigt, fractional Voigt, Jeffrey, Zener, and fractional Zener (Klatt et al., 2007, 2010a; Liu et al., 2014; Kohandel et al., 2005; Okamoto et al., 2011; Holten-Andersen et al., 2014). An overview of the scheme, and the complex modulus function of these rheological models are shown in Table 2.

The merit function for the optimization algorithm was chosen to be the square root of the Residual Sum of Squares, RSS, computed as

$$RSS = \sum_{k=1}^{n} (\mu_{k,fit} - \mu_{k,exp})^{2}$$
 (3)

thus representing the sum of the square difference between the theoretical and experimental values of the complex modulus for all the n sampled frequencies.

### 2.5. Statistical analysis

The storage and loss moduli were computed for each gelatin sample as the average optimized value along 4 equispaced angles: Lilliefors tests rejected data normality for the data populations at each frequency, concentration and magnetic field intensities, so non-parametric tests were adopted and performed with MATLAB version 2016b. The level of significance was set to p=0.05 for all the statistical tests performed, which included a one-way ANOVA for different gelatin concentrations, same excitation frequency and magnetic field, and also another one-way ANOVA for different excitation frequency but same gelatin concentration and magnetic field. A Wilcoxon rank-sum (Mann-Whitney) test was performed to compare data from 0.5 T to 11.7 T scanners.

#### 3. Results and discussion

More than 90% of the data did not show any significant difference among magnetic field strengths (see Table 3): based on this observation the storage modulus values for all frequencies and gelatin concentrations at 0.5 T were comparable with the ones at 11.7 T, and same applied to loss modulus data except for the lowest concentration (p-value <0.05 at 5% w/v). However, for low gelatin concentrations the number of visible wavelength is reduced due to high attenuation.

MRE using the tabletop system was able to detect differences of complex shear moduli for different gelatin concentrations considered at all excitation frequencies: indeed, the real part and magnitude were

**Table 2**Rheological models: graphical depiction and complex modulus as a function of excitation frequency.

Model	Scheme	Complex modulus
Maxwell (Roylance, 2001)	η	$\mu j\omega\eta \over j\omega\eta + \mu$
Springpot (Yasar et al., 2013; Liu et al., 2014; Posnansky et al., 2012)	$O \longrightarrow O$	$\mu_a^{1-a}(j\omega\mu_0)^a$
Voigt (Liu et al., 2014)		$\mu + j\omega\eta$
Zener (Zener, 1948)	, , , , , , , , , , , , , , , , , , ,	$\mu_2 \frac{1+d(j\omega\tau)}{1+j\omega\tau}  \left[ d = \frac{\mu_1+\mu_2}{\mu_2}  ,  \tau = \frac{\eta}{\mu_1} \right]$
Jeffrey (Rudolph and Osswald, 2014)		$-\ \omega\eta_1\frac{\omega\eta_2-j\mu}{\mu+j\omega(\eta_1+\eta_2)}$
Frac Voigt (Yasar et al., 2013; Liu et al., 2014)	- Γ. α α α α α α α α α α α α α α α α α α	$\mu + \mu \left( rac{j\omega\mu_{lpha}}{\mu}  ight)^a$
Frac Zener (Okamoto et al., 2011)	ν <sub>α</sub> , α μ <sub>1</sub> π <sub>1</sub> α μ <sub>2</sub> α μ <sub>2</sub> α μ <sub>3</sub> α μ <sub>4</sub> α μ <sub>4</sub> α μ <sub>5</sub> α μ	$\mu_2 \frac{1+d(j\omega\tau)^a}{1+(j\omega\tau)^a}  \left[ d = \frac{\mu_1+\mu_2}{\mu_2}  ,  \tau = \frac{\mu_a}{\mu_1} \right]$

**Table 3**Comparison of the complex modulus values between 0.5 T and 11.7 T at specific concentrations and excitation frequencies by means of the p-value.

	1000 Hz		2000 Hz			
	Real	Imaginary	Magnitude	Real	Imaginary	Magnitude
5%	0.07	0.14	0.07	0.07	0.04	0.25
10%	0.27	0.80	0.27	0.19	0.57	0.19
15%	0.10	0.10	0.10	0.57	0.10	0.57

different in all the cases, specifically denoting an increase in stiffness corresponding to increasing gelatin concentrations. On the other hand, 75% of the imaginary part values did not exhibit differences, which suggests that the damping characteristics are less sensitive to gel concentrations. Values for real and imaginary parts of the complex shear modulus are reported in Fig. 2 for different excitation frequencies and gelatin concentrations at 0.5, 9.4 and 11.7 T, respectively. A slight but not significant increasing trend in complex shear moduli was detected for increasing frequencies.

An example of Coefficient of Variation (CV) computation is reported for the same gelatin concentration (10%) and excitation frequency (2000 Hz). Examples of displacement magnitude image used for CV calculation are represented in Fig. 3 (with both 0.5 T and 11.7 T scanner) where blue and yellow colors refer to in- and out-of-plane displacement, respectively. CV values at 2000 Hz for a 10% gelatin were 0.5970 for the tabletop scanner and 0.2302 for the high-field scanner. Although in the same order of magnitude, CV values reveal higher SNR in the images from high-field scanner as expected from the monotonic increasing dependency of MR signal on the static magnetic field.

Fig. 4 illustrates both the experimental data at 0.5 T and the fitting results for the models reported in Table 2. Values of the fitted parameters and computed errors are found in Table 4, subdivided for gelatin concentration.

The best performing models are Zener and its fractional version, which display identical errors except for at 10% concentration, and the Jeffrey model, which outperforms the others for the 10% gelatin. In three out of four analyzed gelatin concentrations, the fractional Zener is

equivalent to the Zener model as can be deduced by the value of the fractional coefficient ( $\alpha = 1$ ) (IV parameter in Table 4).

This is in agreement with previous studies performed in brain and liver tissues (Klatt et al., 2007), where the Zener model has shown to provide the best agreement between fit and experimental data among the 3-parameter models in a lower frequency range than the one used in this study. The Zener model parameters were also highly reproducible, while the fractional Zener model fit parameters scattered in a wide range in follow-up studies and provided only an equal or marginally better fit quality in individual experiments.

The imaginary part of the Maxwell model fitting always showed a broad peak for low frequency values, resulting in generally high errors, while the higher order Jeffrey model fitting had a narrower peak in a lower frequency regime, thus generally impacting less the optimization error.

Maxwell and Voigt models generally show higher fitting errors since the lower number of parameters is unable to follow data dynamics.

Indeed, Maxwell and Voigt models can be seen as subsets of more complex models such as the Zener model (Parker et al., 2019): while the Voigt model can be interpreted as a low-frequency approximation to the Zener model, the Maxwell model can be interpreted as its high-frequency approximation, which could would make them appropriate models for specific frequency ranges.

The Fractional Voigt model provided lower errors with respect to the non-fractional equivalent, benefiting from the additional fractional parameter.

Springpot and fractional Voigt models follow data variability at all concentrations with average error values.

Table 4 also shows an increasing trend for the fitted parameters with concentration, in particular for the parameters corresponding to  $\mu$  and  $\eta$  coherently with their physical meaning.

As can be seen in Fig. 4, the gelatin samples show a large variability in the estimation of the shear moduli. We hypothesize that this could be explained by the lack of a standardization process in the production of the samples, by the temperature variations in the scanner room and by the estimation errors provided by the fitting algorithm (approximately

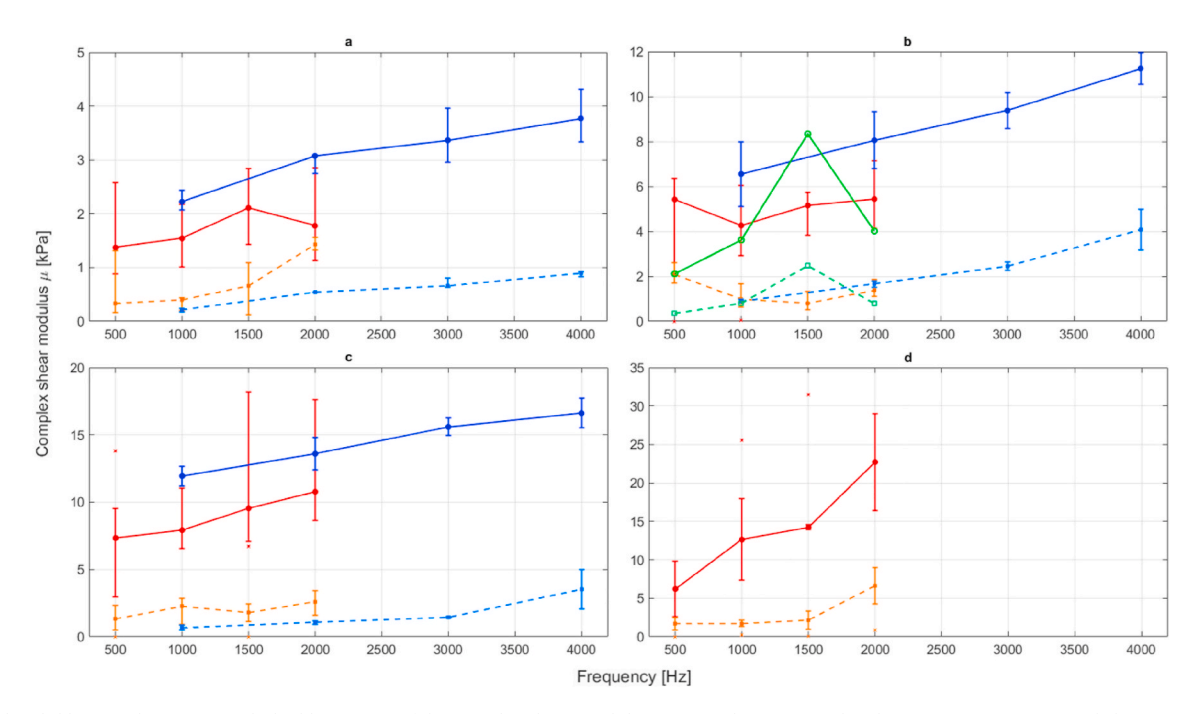


Fig. 2. Real (solid line) and imaginary (dashed line) parts of the complex shear modulus estimated at 0.5 T (red and orange), 9.4 T (green and chartreuse) and 11.7 T (blue and light blue) from the gelatin samples at different concentrations: 5% w/v (a), 10% w/v (b), 15% w/v (c) and 20% w/v (d). Points represent the median values while error bars define population minimum and maximum values at each frequency. Outliers (represented as crosses) were chosen as the data points having an imaginary part of the complex shear modulus equal to zero or with a difference of more than an order of magnitude with respect to the median value.

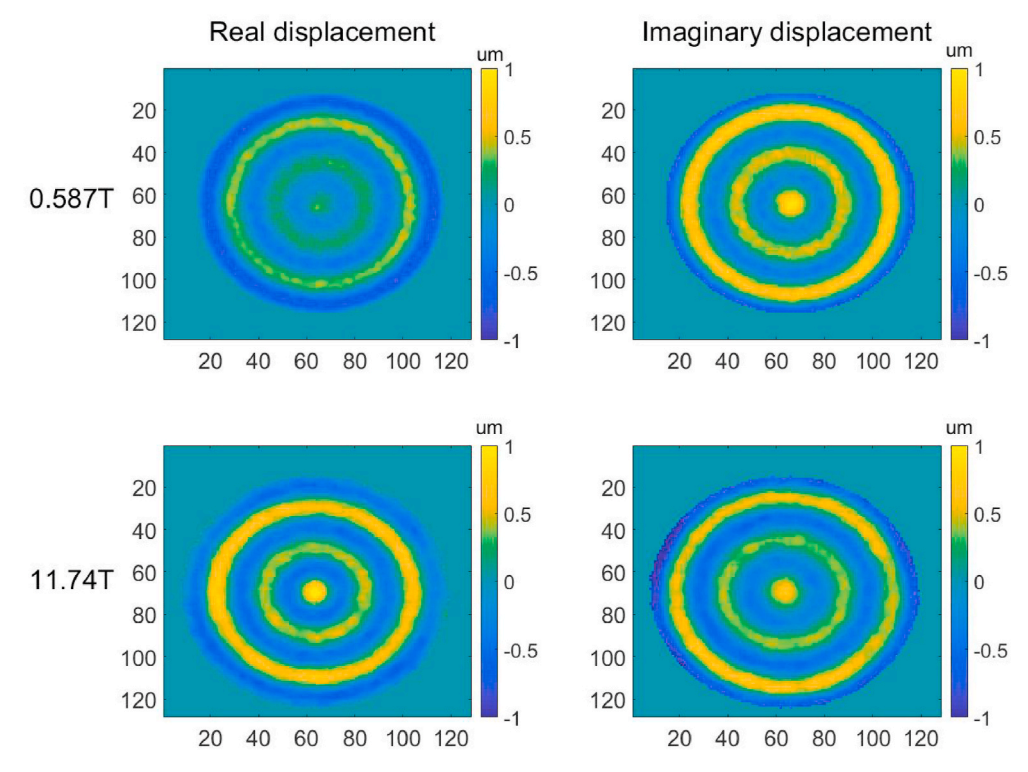


Fig. 3. Real and imaginary part of the complex displacement at 2000 Hz for a 10% gelatin concentration imaged at 0.5 T (a) and at 11.7 T (b).

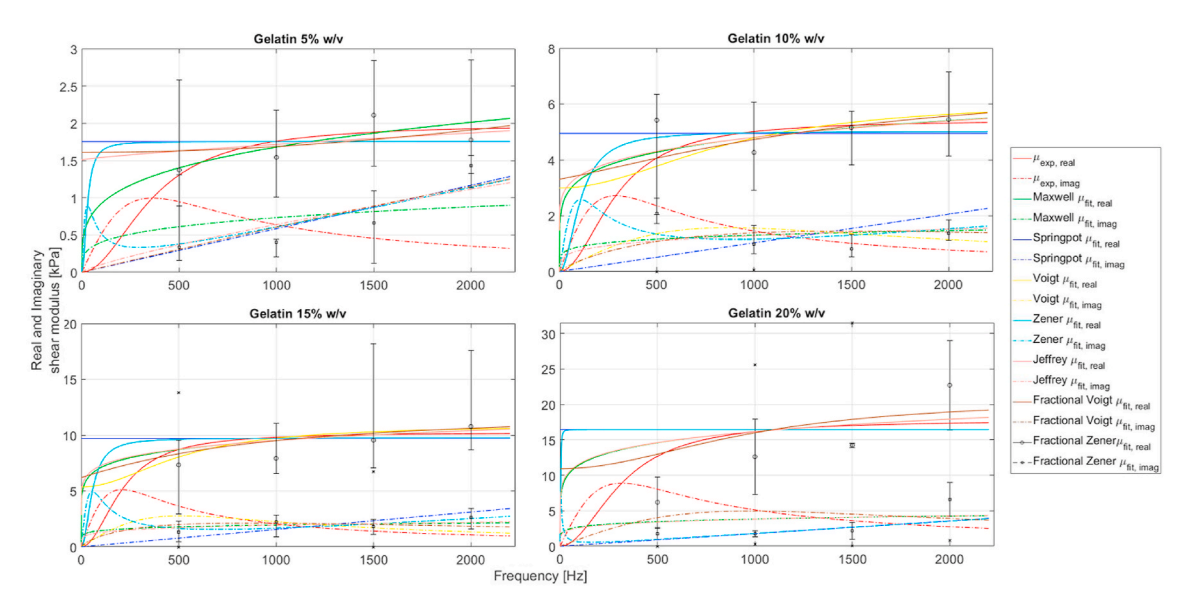


Fig. 4. Experimental values for complex moduli (storage modulus: circles - loss modulus: squares) and fitted curves based on the rheological modeling results in Table 4. Some of the models perform similarly and appear overlapped for the following cases and gelatin concentrations: Zener and Maxwell at 10%, Zener and its fractional version at all concentrations where  $\alpha$  was estimated at 1, the imaginary parts for Zener and Voigt at 5%, Springpot and fractional Voigt at 10% and 20%.

## 5-10%).

In our setup, samples with diameters up to 10 mm can be scanned, which thus require higher frequencies of the piezoelectric actuator to be visualized (Manduca et al., 2021). Although the excitation frequencies applied do not match those for in vivo tissue analysis, which are found in the 50–400 Hz range (Tang et al., 2015; Glaser et al., 2012), these have been previously used for the characterization and study of the diagnostic potential of neurodegeneration in mouse models (Majumdar and Klatt, 2021). Also, this study could be extended for small-scale MRI scanners for other preclinical analysis and imaging of ex vivo human tissue samples such as biopsy samples. Therefore, this study represents a

validation study of the new low-cost MRE system, in line with prior studies that compared tissue mechanical properties across MRE systems (Brinker et al., 2018; Yasar et al., 2013; Liu et al., 2014; Klatt et al., 2010b). Further studies are needed to identify the best suited model for tissue and phantom modeling. Indeed, the use of a wide range of frequencies densely sampled especially in the low frequency range is suggested to improve rheological model fitting and, consequently, parameter estimation. It is a limitation of the presented study that the analysis of earlier collected data using the high field scanners was performed retrospectively and with a limited sample size. Therefore, there is a limited overlapping in the excitation frequency ranges. A thorough

**Table 4**Values of model parameters fit to experimental data at 0.5T with units as follows:

I: η [Pa·s]	II: μ [Pa]			(Maxwell)	-
I: α [-]	II: $\mu_{\alpha}$ [Pa]			(Springpo	t*);
I: η [Pa·s]	II: μ [Pa]			(Voigt);	
I: η [Pa·s]	II: $\mu_1$ [Pa]	III: $\mu_2$ [Pa]		(Zener);	
I: $\eta_1$ [Pa·s]	II: $\eta_2$ [Pa·s]	III: μ [Pa]		(Jeffrey);	
I: μ [Pa]	II: $\mu_{\alpha}$ [Pa·s]	III: α [-]		(Fractional Voigt);	
I: $\mu_{\alpha}$ [Pa·s]	II: $\mu_1$ [Pa]	III: $\mu_2$ [Pa]	IV: α [-]	(Fractional Zener).	
5%	I	II	Ш	IV	$\sqrt{\text{RSS}}$
Maxwell	8.729e-1	1.989e3			3.92
Springpot	2.617e-1	1.183e3			3.22
Voigt	9.286e-2	1.752e3			3.09
Zener	9.782e-2	4.704e3	1.608e3		3.04
Jeffrey	9.877	8.943e-2	1.786e3		3.09
Voigt frac	1.507e3	8.752e-2	7.994e-1		3.05
Zener frac	9.782e-2	4.704e3	1.608e3	1.000	3.04
10%	I	П	III	IV	$\sqrt{\text{RSS}}$
Maxwell	3.945	5.151e3			6.21
Springpot	1.472e-1	4.713e3			6.04
Voigt	1.243e-1	4.869e3			6.58
Zener	3.945	5.151e3	4.698e-4		6.21
Jeffrey	5.644	6.599e-2	5.126e3		5.90
Voigt frac	4.546e2	9.998e4	1.617e-1		6.05
Zener frac	4.227	7.515e3	6.447e-4	4.102e-1	6.01
15%	I	II	Ш	IV	√RSS
Maxwell	9.877	1.006e4			17.4
Springpot	1.328e-1	1.051e4			16.1
Voigt	2.087e-1	9.760e3			17.0
Zener	4.876e-1	4.708e3	7.983e3		15.8
Jeffrev	2.683e1	1.602e-1	9.923e3		16.9
Voigt frac	3.922e3	4.541	2.158e-1		16.1
Zener frac	4.876e-1	4.708e3	7.983e3	1.000	15.8
20%	I	II	III	IV	$\sqrt{\text{RSS}}$
Maxwell	8.926	1.778e4			32.4
Springpot	1.481e-1	1.968e4			31.1
Voigt	2.836e-1	1.645e4			33.2
Zener	1.616	9.911e3	1.093e4		29.8
Jeffrey	9.998e2	2.800e-1	1.646e4		33.2
Voigt frac	1.806e3	9.976e4	1.652e-1		31.1

(\*) In Springpot model an additional parameter  $\mu_0$  was considered and kept constant to the value of 1 Pa·s.

study with a greater match between frequencies used at low and high field scanners and simulations replicating the experimental conditions should be performed to better validate the results presented in this study.

## 4. Conclusion

An MRE characterization of gelatin phantoms dynamic properties using a compact low field scanner was presented. Complex shear stiffness values were comparable when processed from images acquired with the tabletop low field scanner and an 11.7 T scanner, while the Coefficient of Variation of the former was double. Nevertheless, MRE on the tabletop system is capable of detecting differences of complex shear moduli for increasing gelatin concentrations. This indicates the feasibility of future low-cost MRE experiments on ex-vivo samples for the characterization of tissue in both normal and pathological states. The Springpot model provides the best fit among the 2-parameter models while this is the case for the Zener model among the 3-parameter models. The addition of a further parameter in the fractional Zener model improved the fit quality only at one of the four concentrations.

#### **Author statement**

**Marco Andrea Zampini**: Conceptualization, Methodology, Software, Validation, Formal analysis, Data Curation, Writing – Original Draft, Writing – Review & Editing, Visualization.

**Martina Guidetti**: Conceptualization, Methodology, Software, Validation, Formal analysis, Data Curation, Writing – Original Draft, Writing – Review & Editing, Visualization.

**Thomas J. Royston**: Conceptualization, Methodology, Writing – Original Draft, Writing – Review & Editing, Supervision, Project administration, Funding acquisition.

**Dieter Klatt**: Conceptualization, Methodology, Writing – Original Draft, Writing – Review & Editing, Supervision, Project administration, Funding acquisition.

## **Declaration of competing interest**

The authors declare that they have no known competing financial interests or personal relationships that could have appeared to influence the work reported in this paper.

## Acknowledgments

Research supported by NSF Grant No. 1852691 and NIH Grant No. AR071162.

#### References

Amador, C., Urban, M.W., Chen, S., Chen, Q., An, K.-N., Greenleaf, J.F., 2011. Shear elastic modulus estimation from indentation and sduv on gelatin phantoms. IEEE (Inst. Electr. Electron. Eng.) Trans. Biomed. Eng. 58 (6), 1706–1714.

Bagley, R.L., Torvik, P., 1983. A theoretical basis for the application of fractional calculus to viscoelasticity. J. Rheol. 27 (3), 201–210.

Bahn, M.M., Brennan, M.D., Bahn, R.S., Dean, D.S., Kugel, J.L., Ehman, R.L., 2009. Development and application of magnetic resonance elastography of the normal and pathological thyroid gland in vivo. J. Magn. Reson. Imag.: Off. J. Int. Soc. Magn. Reson. Med. 30 (5), 1151–1154.

Balleyguier, C., Lakhdar, A.B., Dunant, A., Mathieu, M.-C., Delaloge, S., Sinkus, R., 2018.
Value of whole breast magnetic resonance elastography added to mri for lesion characterization. NMR Biomed. 31 (1), e3795.

Basford, J.R., Jenkyn, T.R., An, K.-N., Ehman, R.L., Heers, G., Kaufman, K.R., 2002. Evaluation of healthy and diseased muscle with magnetic resonance elastography. Arch. Phys. Med. Rehabil. 83 (11), 1530–1536.

Bottomley, P.A., Foster, T.H., Argersinger, R.E., Pfeifer, L.M., 1984. A review of normal tissue hydrogen nmr relaxation times and relaxation mechanisms from 1–100 mhz: dependence on tissue type, nmr frequency, temperature, species, excision, and age. Med. Phys. 11 (4), 425–448.

Braun, J., Tzschätzsch, H., Körting, C., Ariza de Schellenberger, A., Jenderka, M., Drießle, T., Ledwig, M., Sack, I., 2018. A compact 0.5 t mr elastography device and its application for studying viscoelasticity changes in biological tissues during progressive formalin fixation. Magn. Reson. Med. 79 (1), 470–478.

Brinker, S., Klatt, D., 2016. Demonstration of concurrent tensile testing and magnetic resonance elastography. J. Mech. Behav. Biomed. Mater. 63, 232–243.

Brinker, S.T., Kearney, S.P., Royston, T.J., Klatt, D., 2018. Simultaneous magnetic resonance and optical elastography acquisitions: comparison of displacement images and shear modulus estimations using a single vibration source. J. Mech. Behav. Biomed. Mater. 84, 135–144.

Cabrelli, L.C., Grillo, F.W., Sampaio, D.R., Carneiro, A.A., Pavan, T.Z., 2017. Acoustic and elastic properties of glycerol in oil-based gel phantoms. Ultrasound Med. Biol. 43 (9), 2086–2094.

Cao, Y., Li, G.-Y., Zhang, X., Liu, Y.-L., 2017. Tissue-mimicking materials for elastography phantoms: a review. Extrem. Mech. Lett. 17, 62–70.

Chen, Q., Suki, B., An, N., 2003. Dynamic mechanical properties of agarose gel by a fractional derivative model. In: Proc. Summer Bioengineering Conf., Sonesta Beach Resort, Key Biscayne. Florida, USA, 25–29 June.

Culjat, M.O., Goldenberg, D., Tewari, P., Singh, R.S., 2010. A review of tissue substitutes for ultrasound imaging. Ultrasound Med. Biol. 36 (6), 861–873.

Deffieux, T., Gennisson, J.-L., Bercoff, J., Tanter, M., 2011. On the effects of reflected waves in transient shear wave elastography. IEEE Trans. Ultrason. Ferroelectrics Freq. Contr. 58 (10), 2032–2035.

Doyley, M.M., Bamber, J.C., Fuechsel, F., Bush, N.L., 2001. A freehand elastographic imaging approach for clinical breast imaging: system development and performance evaluation. Ultrasound Med. Biol. 27 (10), 1347–1357.

Dutt, V., Kinnick, R.R., Muthupillai, R., Oliphant, T.E., Ehman, R.L., Greenleaf, J.F., 2000. Acoustic shear-wave imaging using echo ultrasound compared to magnetic resonance elastography. Ultrasound Med. Biol. 26 (3), 397–403.

- Emelianov, S., Lubinski, M., Weitzel, W., Wiggins, R., Skovoroda, A., O'donnell, M., 1995. Elasticity imaging for early detection of renal pathology. Ultrasound Med. Biol. 21 (7), 871–883.
- Gennisson, J.-L., Deffieux, T., Fink, M., Tanter, M., 2013. Ultrasound elastography: principles and techniques. Diagn. Intervent. Imag. 94 (5), 487–495.
- Glaser, K.J., Manduca, A., Ehman, R.L., 2012. Review of mr elastography applications and recent developments. J. Magn. Reson. Imag. 36 (4), 757–774.
- Guidetti, M., Royston, T.J., 2018. Analytical solution for converging elliptic shear wave in a bounded transverse isotropic viscoelastic material with nonhomogeneous outer boundary. J. Acoust. Soc. Am. 144 (4), 2312–2323.
- Guidetti, M., Lorgna, G., Klatt, D., Vena, P., Royston, T.J., 2019. Anisotropic composite material phantom to improve skeletal muscle characterization using magnetic resonance elastography. J. Mech. Behav. Biomed. Mater. 89, 199–208.
- Hall, T.J., Bilgen, M., Insana, M.F., Krouskop, T.A., 1997. Phantom materials for elastography. IEEE Trans. Ultrason. Ferroelectrics Freq. Contr. 44 (6), 1355–1365.
- Hamhaber, U., Grieshaber, F., Nagel, J., Klose, U., 2003. Comparison of quantitative shear wave mr-elastography with mechanical compression tests. Magn. Reson. Med.: Off. J. Int. Soc. Magn. Reson. Med. 49 (1), 71–77.
- Hiscox, L.V., Johnson, C.L., McGarry, M.D., Perrins, M., Littlejohn, A., van Beek, E.J., Roberts, N., Starr, J.M., 2018. High-resolution Mr Elastography Reveals Differences in Subcortical Gray Matter Viscoelasticity between Young and Healthy Older Adults. Neurobiol. Aging 65, 158–167.
- Holten-Andersen, N., Jaishankar, A., Harrington, M.J., Fullenkamp, D.E., DiMarco, G., He, L., McKinley, G.H., Messersmith, P.B., Lee, K.Y.C., 2014. Metal-coordination: using one of nature's tricks to control soft material mechanics. J. Mater. Chem. B 2 (17), 2467–2472.
- Hughes, J.D., Fattahi, N., Van Gompel, J., Arani, A., Meyer, F., Lanzino, G., Link, M.J., Ehman, R., Huston, J., 2015. Higher-resolution magnetic resonance elastography in meningiomas to determine intratumoral consistency. Neurosurgery 77 (4), 653–659.
- Ipek-Ugay, S., Drießle, T., Ledwig, M., Guo, J., Hirsch, S., Sack, I., Braun, J., 2015. Tabletop magnetic resonance elastography for the measurement of viscoelastic parameters of small tissue samples. J. Magn. Reson. 251, 13–18.
- Kearney, S.P., Majumdar, S., Royston, T.J., Klatt, D., 2017. Simultaneous 3d mr elastography of the in vivo mouse brain. Phys. Med. Biol. 62 (19), 7682.
- Kemper, J., Sinkus, R., Lorenzen, J., Nolte-Ernsting, C., Stork, A., Adam, G., 2004. Mr elastography of the prostate: initial in-vivo application. In: RöFo-Fortschritte auf dem Gebiet der Röntgenstrahlen und der bildgebenden Verfahren, vol. 176. © Georg Thieme Verlag KG Stuttgart., New York, pp. 1094–1099.
- Khan, A.A., Kearney, S.P., Royston, T.J., 2018. Finite element based optimization of human fingertip optical elastography. J. Eng. Sci. Med. Diagn. Ther. 1 (3), 031007.
- Kiss, M.Z., Varghese, T., Hall, T.J., 2004. Viscoelastic characterization of in vitro canine tissue. Phys. Med. Biol. 49 (18), 4207.
- Klatt, D., Hamhaber, U., Asbach, P., Braun, J., Sack, I., 2007. Noninvasive assessment of the rheological behavior of human organs using multifrequency mr elastography: a study of brain and liver viscoelasticity. Phys. Med. Biol. 52 (24), 7281.
- Klatt, D., Papazoglou, S., Braun, J., Sack, I., 2010a. Viscoelasticity-based mr elastography of skeletal muscle. Phys. Med. Biol. 55 (21), 6445.
- Klatt, D., Friedrich, C., Korth, Y., Vogt, R., Braun, J., Sack, I., 2010b. Viscoelastic properties of liver measured by oscillatory rheometry and multifrequency magnetic resonance elastography. Biorheology 47 (2), 133–141.
- Klatt, D., Yasar, T.K., Royston, T.J., Magin, R.L., 2013. Sample interval modulation for the simultaneous acquisition of displacement vector data in magnetic resonance elastography: theory and application. Phys. Med. Biol. 58 (24), 8663.
- Kohandel, M., Sivaloganathan, S., Tenti, G., Darvish, K., 2005. Frequency dependence of complex moduli of brain tissue using a fractional zener model. Phys. Med. Biol. 50 (12), 2799.
- Kolipaka, A., McGee, K.P., Araoz, P.A., Glaser, K.J., Manduca, A., Ehman, R.L., 2009. Evaluation of a rapid, multiphase mre sequence in a heart-simulating phantom. Magn. Reson. Med.: Off. J. Int. Soc. Magn. Reson. Med. 62 (3), 691–698.
- Krouskop, T., Dougherty, D., Vinson, F., et al., 1987. A pulsed Doppler ultrasonic system for making noninvasive measurements of the mechanical properties of soft tissue. J. Rehabil. Res. Dev. 24 (2), 1–8.
- Ladd, M.E., 2007. High-field-strength magnetic resonance: potential and limits. Top. Magn. Reson. Imag. 18 (2), 139–152.
- Larin, K.V., Sampson, D.D., 2017. Optical coherence elastography–oct at work in tissue biomechanics. Biomed. Opt Express 8 (2), 1172–1202.
- Lee, C.U., Glockner, J.F., Glaser, K.J., Yin, M., Chen, J., Kawashima, A., Kim, B., Kremers, W.K., Ehman, R.L., Gloor, J.M., 2012. Mr elastography in renal transplant patients and correlation with renal allograft biopsy: a feasibility study. Acad. Radiol. 19 (7), 834–841.
- Liang, X., Boppart, S.A., 2009. Biomechanical properties of in vivo human skin from dynamic optical coherence elastography. IEEE (Inst. Electr. Electron. Eng.) Trans. Biomed. Eng. 57 (4), 953–959.
- Liu, Y., Yasar, T.K., Royston, T.J., 2014. Ultra wideband (0.5–16 khz) mr elastography for robust shear viscoelasticity model identification. Phys. Med. Biol. 59 (24), 7717.
- Low, G., Kruse, S.A., Lomas, D.J., 2016. General review of magnetic resonance elastography. World J. Radiol. 8 (1), 59.
- Maccabi, A., Shin, A., Namiri, N.K., Bajwa, N., John, M.S., Taylor, Z.D., Grundfest, W., Saddik, G.N., 2018. Quantitative characterization of viscoelastic behavior in tissuemimicking phantoms and ex vivo animal tissues. PloS One 13 (1), e0191919.
- Madsen, E.L., Frank, G.R., Apr. 29 1997. Very low scatter liquid and solid tissue mimicking material for ultrasound phantoms and method of making the same. uS Patent 5, 625, 137.
- Madsen, E., Frank, G., Krouskop, T., Varghese, T., Kallel, F., Ophir, J., 2003. Tissue-mimicking oil-in-gelatin dispersions for use in heterogeneous elastography phantoms. Ultrason. Imag. 25 (1), 17–38.

- Madsen, E.L., Hobson, M.A., Shi, H., Varghese, T., Frank, G.R., 2005. Tissue-mimicking agar/gelatin materials for use in heterogeneous elastography phantoms. Phys. Med. Biol. 50 (23), 5597.
- Manduca, A., Oliphant, T.E., Dresner, M.A., Mahowald, J., Kruse, S.A., Amromin, E., Felmlee, J.P., Greenleaf, J.F., Ehman, R.L., 2001. Magnetic resonance elastography: non-invasive mapping of tissue elasticity. Med. Image Anal. 5 (4), 237–254.
- Majumdar, S., Klatt, D., 2021. Longitudinal study of sub-regional cerebral viscoelastic properties of 5xfad alzheimer's disease mice using multifrequency mr elastography. Magn. Reson. Med. 86 (1), 405–414.
- Manduca, A., Bayly, P.J., Ehman, R.L., Kolipaka, A., Royston, T.J., Sack, I., Sinkus, R., Van Beers, B.E., 2021. Mr elastography: principles, guidelines, and terminology. Magn. Reson. Med. 85 (5), 2377–2390.
- Mori, Y., Tokura, H., Yoshikawa, M., 1997. Properties of hydrogels synthesized by freezing and thawing aqueous polyvinyl alcohol solutions and their applications. J. Mater. Sci. 32 (2), 491–496.
- Mun, H.S., Choi, S.H., Kook, S.H., Choi, Y., Jeong, W.K., Kim, Y., 2013. Validation of intra-and interobserver reproducibility of shearwave elastography: phantom study. Ultrasonics 53 (5), 1039–1043.
- Muthupillai, R., Lomas, D., Rossman, P., Greenleaf, J.F., Manduca, A., Ehman, R.L., 1995. Magnetic resonance elastography by direct visualization of propagating acoustic strain waves. Science 269 (5232), 1854–1857.
- Nguyen, K.-C.T., Le, L.H., Tran, T.N., Sacchi, M.D., Lou, E.H., 2014. Excitation of ultrasonic lamb waves using a phased array system with two array probes: phantom and in vitro bone studies. Ultrasonics 54 (5), 1178–1185.
- Okamoto, R., Clayton, E., Bayly, P., 2011. Viscoelastic properties of soft gels: comparison of magnetic resonance elastography and dynamic shear testing in the shear wave regime. Phys. Med. Biol. 56 (19), 6379.
- Ortiz, J.E., Lagos, R., 2015. A viscoelastic model to simulate soft tissue materials. In: Journal of Physics: Conference Series, vol. 633. IOP Publishing, 012099.
- Oudry, J., Bastard, C., Miette, V., Willinger, R., Sandrin, L., 2009. Copolymer-in-oil phantom materials for elastography. Ultrasound Med. Biol. 35 (7), 1185–1197.
- Parker, K., Huang, S., Musulin, R., Lerner, R., 1990. Tissue response to mechanical vibrations for "sonoelasticity imaging". Ultrasound Med. Biol. 16 (3), 241–246.
- Parker, K., Szabo, T., Holm, S., 2019. Towards a consensus on rheological models for elastography in soft tissues. Phys. Med. Biol. 64 (21), 215012.
- Pavan, T.Z., Madsen, E.L., Frank, G.R., Carneiro, A.A.O., Hall, T.J., 2010. Nonlinear elastic behavior of phantom materials for elastography. Phys. Med. Biol. 55 (9), 2679.
- Plewes, D., Betty, I., Urchuk, S., Soutar, I., 1995. Visualizing tissue compliance with mr imaging. J. Magn. Reson. Imag. 5 (6), 733–738.
- Plewes, D.B., Bishop, J., Samani, A., Sciarretta, J., 2000. Visualization and quantification of breast cancer biomechanical properties with magnetic resonance elastography. Phys. Med. Biol. 45 (6), 1591.
- Posnansky, O., Guo, J., Hirsch, S., Papazoglou, S., Braun, J., Sack, I., 2012. Fractal network dimension and viscoelastic powerlaw behavior: I. a modeling approach based on a coarse-graining procedure combined with shear oscillatory rheometry. Phys. Med. Biol. 57 (12), 4023.
- Pritz, T., 2003. Five-parameter fractional derivative model for polymeric damping materials. J. Sound Vib. 265 (5), 935–952.
- Quan, K., Christison, G., MacKenzie, H., Hodgson, P., 1993. Glucose determination by a pulsed photoacoustic technique: an experimental study using a gelatin-based tissue phantom. Phys. Med. Biol. 38 (12), 1911.
- Reiter, R., Majumdar, S., Kearney, S., Kajdacsy-Balla, A., Macias, V., Crivellaro, S., Caldwell, B., Abern, M., Royston, T.J., Klatt, D., 2020. Prostate cancer assessment using mr elastography of fresh prostatectomy specimens at 9.4 t. Magn. Reson. Med. 84 (1), 396–404.
- Ringleb, S.I., Chen, Q., Lake, D.S., Manduca, A., Ehman, R.L., An, K.-N., 2005.
  Quantitative shear wave magnetic resonance elastography: comparison to a dynamic shear material test. Magn. Reson. Med.: Off. J. Int. Soc. Magn. Reson. Med. 53 (5), 1197–1201.
- Roylance, D., 2001. Engineering Viscoelasticity, vol. 2139. Department of Materials Science and Engineering–Massachusetts Institute of Technology, Cambridge MA, pp. 1–37.
- Rudolph, N., Osswald, T.A., 2014. Polymer Rheology: Fundamentals and Applications. Carl Hanser Verlag GmbH Co KG.
- Sack, I., Rump, J., Elgeti, T., Samani, A., Braun, J., 2009. Mr elastography of the human heart: noninvasive assessment of myocardial elasticity changes by shear wave amplitude variations. Magn. Reson. Med.: Off. J. Int. Soc. Magn. Reson. Med. 61 (3), 668–677.
- Sack, I., Jöhrens, K., Würfel, J., Braun, J., 2013. Structure-sensitive elastography: on the viscoelastic powerlaw behavior of in vivo human tissue in health and disease. Soft Matter 9 (24), 5672–5680.
- Sarvazyan, A., J Hall, T., W Urban, M., Fatemi, M., R Aglyamov, S., Garra, B.S., 2011. An overview of elastography-an emerging branch of medical imaging. Curr. Med. Imag. Rev. 7 (4), 255–282.
- Sarvazyan, A.P., Urban, M.W., Greenleaf, J.F., 2013. Acoustic waves in medical imaging and diagnostics. Ultrasound Med. Biol. 39 (7), 1133–1146.
- Taljanovic, M.S., Gimber, L.H., Becker, G.W., Latt, L.D., Klauser, A.S., Melville, D.M., Gao, L., Witte, R.S., 2017. Shear-wave elastography: basic physics and musculoskeletal applications. Radiographics 37 (3), 855–870.
- Talwalkar, J.A., 2008. Elastography for detecting hepatic fibrosis: options and considerations. Gastroenterology 135 (1), 299.
- Tang, A., Cloutier, G., Szeverenyi, N.M., Sirlin, C.B., 2015. Ultrasound elastography and mr elastography for assessing liver fibrosis: part 1, principles and techniques. Am. J. Roentgenol. 205 (1), 22–32.

- Taylor, L.S., Lerner, A.L., Rubens, D.J., Parker, K.J., 2002. A kelvin-voight fractional derivative model for viscoelastic characterization of liver tissue. In: ASME 2002 International Mechanical Engineering Congress and Exposition. American Society of Mechanical Engineers Digital Collection, pp. 447–448.
- Varghese, T., 2009. Quasi-static ultrasound elastography. Ultrasound Clin. 4 (3), 323.
  Vieira, S.L., Pavan, T.Z., Junior, J.E., Carneiro, A.A., 2013. Paraffin-gel tissue-mimicking material for ultrasound-guided needle biopsy phantom. Ultrasound Med. Biol. 39 (12), 2477–2484.
- Von Gierke, H.E., Oestreicher, H.L., Franke, E.K., Parrack, H.O., von Wittern, W.W., 1952. Physics of vibrations in living tissues. J. Appl. Physiol. 4 (12), 886–900.
- Wang, M., Byram, B., Palmeri, M., Rouze, N., Nightingale, K., 2013. Imaging transverse isotropic properties of muscle by monitoring acoustic radiation force induced shear waves using a 2-d matrix ultrasound array. IEEE Trans. Med. Imag. 32 (9), 1671–1684.
- Xu, L., Lin, Y., Han, J., Xi, Z., Shen, H., Gao, P., 2007. Magnetic resonance elastography of brain tumors: preliminary results. Acta Radiol. 48 (3), 327–330.
- Yamakoshi, Y., Sato, J., Sato, T., 1990. Ultrasonic imaging of internal vibration of soft tissue under forced vibration. IEEE Trans. Ultrason. Ferroelectrics Freq. Contr. 37 (2), 45–53.
- Yang, X., Church, C.C., 2006. A simple viscoelastic model for soft tissues the frequency range 6-20 mhz. IEEE Trans. Ultrason. Ferroelectrics Freq. Contr. 53 (8), 1404–1411.
- Yasar, T.K., Royston, T.J., Magin, R.L., 2013. Wideband mr elastography for viscoelasticity model identification. Magn. Reson. Med. 70 (2), 479–489.
- Zell, K., Sperl, J., Vogel, M., Niessner, R., Haisch, C., 2007. Acoustical properties of selected tissue phantom materials for ultrasound imaging. Phys. Med. Biol. 52 (20), NA75
- Zener, C., 1948. Elasticity and Anelasticity of Metals. University of Chicago press. Zhang, W., Chen, H.Y., Kassab, G.S., 2007. A rate-insensitive linear viscoelastic model for soft tissues. Biomaterials 28 (24), 3579–3586.